



Title	Wave-current interaction effects on marine energy converters
Author(s)	Saruwatari, Ayumi; Ingram, David M.; Cradden, Lucy
Citation	Ocean Engineering, 73, 106-118 <a href="https://doi.org/10.1016/j.oceaneng.2013.09.002">https://doi.org/10.1016/j.oceaneng.2013.09.002</a>
Issue Date	2013-11-15
Doc URL	<a href="http://hdl.handle.net/2115/53379">http://hdl.handle.net/2115/53379</a>
Type	article (author version)
File Information	Saruwatari-Ingram-Cradden-submitted.pdf



[Instructions for use](#)

# Wave-Current Interaction Effects on Marine Energy Converters

Ayumi Saruwatari<sup>a,\*</sup>, David M Ingram<sup>b</sup>, Lucy Cradden<sup>b</sup>

<sup>a</sup>Coastal and Offshore Engineering Laboratory, School of Engineering, Hokkaido University, Sapporo, Japan

<sup>b</sup>Institute for Energy Systems, School of Engineering, The University of Edinburgh, Edinburgh EH9 3JL, United Kingdom

---

## Abstract

Many countries have significant interests in generating electricity using waves and tidal current technologies. In energetic areas, waves and tidal currents interact for modifying the energy resource and impacting on the design conditions. Changes to the wave climate depend on the strength of the current and the relative wave direction. SWAN simulations of the wave climate around the Orkney Islands, with and without currents, show that considerable changes in the wave climate occur near sites of interest to wave and tidal energy project developers. Using circular statistics the effect of the relative angle between the waves and the current can be investigated. Local effects can lead to 150-200% increases in wave height when the waves oppose the current. These dramatic changes lead to an increase in wave power of over  $100\text{kWm}^{-1}$ . The complex nature of the tides in the channels also leads to large changes in wave power during the so-called *slack water* period. *Wave amplification diagrams* are proposed to provide a convenient summary of wave-current effects at a particular site and allow a statistical analysis to be made. When performing resource analysis and site selection work for marine energy projects, wave-current interaction must be considered.

**Keywords:** Marine Energy, Resource Assessment, Wave Modelling, SWAN

**2010 MSC:** 76D33, 62P12

---

## 1. Introduction

Currently there is significant interest in the generation of renewable electricity from the oceans, primarily by the conversion of either wave or tidal current energy. Many countries around the world have ambitious plans for exploiting the maritime energy resource to help address their long term (2050) targets for decarbonising their economies. In their 2010 annual report the International Energy Agency's implementing agreement on ocean energy systems states that, (Brito-Melo and Huckerby, 2010)

Ocean energy generation has a potential to reach 3.6 GW of installed capacity by 2020 and close to 188 GW by 2050. This represents over 9 TWh per year by 2020 and over 645 TWh per year by 2050, amounting to 0.3% and 15% of the projected EU-27 electricity demand by 2020 and 2050 respectively.

Bringing this energy to market requires understanding of the available energy resource on three distinct levels (Ingram et al., 2011). Firstly, an *early stage*, high level assessment of the resource at a geographic scale should be conducted. This is used to identify likely areas in which energy projects can be deployed. Secondly, a detailed, *project development*, study, is undertaken to select the individual locations at which machines should be deployed. Finally, *operational* resource monitoring and modelling is required both to forecast energy production and to plan ongoing operation and maintenance work.

At both the *project development* and *operational* levels an understanding of the interaction of the waves and currents is required. This is critical if either wave energy converters or tidal current turbines are to be deployed as in the first case the current will modify the shape and spectra of the waves, while in the second, the unsteady fluctuations in the flow arising from the waves will cause transient loading on the turbine rotor. Whilst in a few locations (for example Strangford Narrows in Northern Ireland) it is possible to find a site with strong tidal currents which is relatively sheltered from waves, the most energetic sites being exam-

---

\*Corresponding Author

Email addresses: saruwata@eng.hokudai.ac.jp (Ayumi Saruwatari), david.ingram@ed.ac.uk (David M Ingram), lucy.cradden@ed.ac.uk (Lucy Cradden)

ined have both highly energetic waves and strong tidal currents. In conducting resource assessments, spectral wave models, e.g. SWAN (Booij et al., 1999; Ris et al., 1999), TOMAWAC (Brière et al., 2007), and MIKE-21 SW (Sørensen et al., 2004) are widely used. These sophisticated, third generation spectral models describe the behaviour of the waves in terms of the two-dimensional wave action density spectrum. The action density spectrum,  $N(\sigma, \theta) = S(\sigma, \theta)/\sigma$ , is used because action density is conserved in the presence of currents, whereas energy is not. The evolution of the wave energy spectrum is described using the spectral action balance equation which includes terms modelling the influence of bathymetry and current. In this paper the structured formulation of the SWAN model (van der Westhuysen et al., 2007) has been used.

The purpose of the study is to characterise how current at a specific locations modifies the wave climate. Such interactions modify the energy available for conversion and, as a direct consequence, the tuning (and possibly design) of a wave energy device deployed at the location. The present study considers the highly energetic waters in the Orkney archipelago and Pentland Firth (Fig. 1). In 2009 this area was the subject of a leasing round by the United Kingdom's Crown Estate which resulted in the granting of 10 leases for a total of about 1.2GW of installed capacity (BVG Associates, 2011). By analysing the differences between SWAN predictions with and without tidal currents, locations at which there are significant changes in the wave environment are identified and the influence of current is summarised through a novel wave amplification diagram §5. Circular statistics and quantile regression are performed on the simulation data to derive diagrams which explain how the effects of the tidal currents on the waves varies with the relative direction between the current and the waves.

## 2. Modelling

### 2.1. Wave Prediction Model

The wave field was computed using the wave prediction model, Simulating Waves Nearshore (SWAN, version 40.85), developed by Delft University of Technology (van der Westhuysen et al., 2007). All parameters in this model are represented using wave action density defined by the following equations.

$$N(\sigma, \theta) = S(\sigma, \theta)/\sigma, \quad (1)$$

$$S(\sigma, \theta) = 2 \int_{-\infty}^{\infty} C(\tau) e^{i\sigma\tau} d\tau, \quad (2)$$

where  $N = N(\sigma, \theta, \mathbf{x}, t)$  is the wave action density,  $\sigma$  is the frequency of the wave (in radians), and  $S$  is the energy density, determined based on a Fourier transform of the auto-covariance function  $C$  of the sea surface elevation. Wave action density is updated by solving the following action balance equation:

$$\frac{\partial N}{\partial t} + \nabla_{\mathbf{x}} \cdot [(\mathbf{c}_g + \mathbf{U})N] + \frac{\partial c_{\sigma} N}{\partial \sigma} + \frac{\partial c_{\theta} N}{\partial \theta} = \frac{S_{tot}}{\sigma}, \quad (3)$$

where  $\theta$  is wave direction,  $\mathbf{c}_g$  is group velocity,  $\mathbf{U}$  is current velocity,  $c_{\sigma}$  and  $c_{\theta}$  are the propagation velocity for  $\sigma$  and  $\theta$  spaces respectively, and  $S_{tot}$  represents the sum of the dissipation and generation of the wave energy (e.g. due to the effects of wind, bottom friction, white capping and so on). The effect of the currents on the wave field is included by changing the wave propagation velocity with the current velocity  $\mathbf{U}$  as described in the above equation, which can reproduce the basic effects of the current on the wave fields, although it is unable to reproduce the non-linear interactions between waves and currents. Wind input and wave dissipation due to wave-wave interaction and white capping were computed by the third generation mode of this model with Westhuysen's formulations (van der Westhuysen et al., 2007) which is known to reproduce the development of the wave field due to wind more accurately. Bottom friction was computed based on JONSWAP formulations and default values were used for the other settings.

One-way nesting using four computational domains (Table 1) was used to account for both swell and wind driven waves developed across the Atlantic Ocean and also to account for deformation due to the rapidly changing local bathymetric conditions around the Orkney islands. Meteorological re-analysis data sets from ERA-Interim ( $1.5^{\circ} \times 1.5^{\circ}$  resolution), provided by European Centre for Medium-Range Weather Forecasts (ECMWF) at a time-step of six hours were used for the wind input for domain 1. Wind data with higher resolution, computed as described in the following section, were input for domains 2–4 every hour. We modelled two cases: (case 1) where the wave field is computed without considering the effects of tidal currents and (case 2) where tidal effects are included. Tidal current velocity and tidal elevations were computed as described in section 2.3 and input into the domain four times every hour. Bathymetry data used in the simulation was taken from the General Bathymetric Chart of the Oceans (GEBCO) global data at a resolution of 30 arc seconds. The computations were performed for a 36 day period covering 2006/July/9, 00:00–2006/August/14, 00:00 (GMT). Throughout this

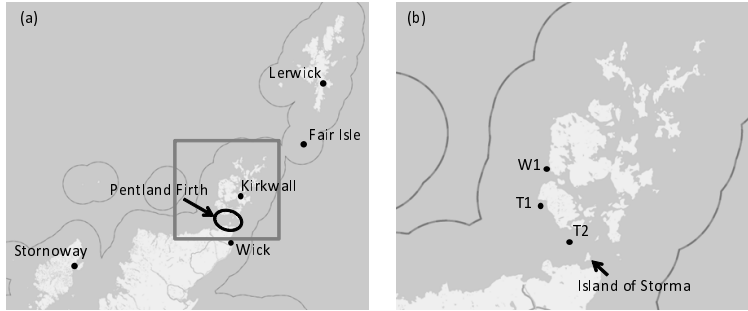


Figure 1: Schematics of Orkney Islands. Points indicate locations of (a) wind data, (b) wave and tidal data. (b is a closeup of a.)

Table 1: Computational domain for SWAN simulation.

Domain	Computational area	Grid number	Grid spacing (lon×lat)	$\Delta t$
1	W70.00°–E10.00°, N41.00°–N69.00°	240×84	0°20′ × 0°20′	10min
2	W15.00°–E5.00°, N57.00°–N63.00°	120×60	0°6′ × 0°6′	10min
3	W6.00°–W2.00°, N58.00°–N60.00°	120×120	0°2′ × 0°1′	10min
4	W3.75°–W2.25°, N58.50°–N59.50°	180×120	0°0′30″ × 0°0′30″	3min

paper the time,  $t$ , is defined relative to the start of the computation at midnight on the 9<sup>th</sup> of July.

## 2.2. Mesoscale Meteorological Model

The Weather Research and Forecasting model (WRF-ARW, version 3.3.1), a mesoscale meteorological model developed by National Center for Atmospheric Research (NCAR), was used for generating high-resolution wind input data over the ocean. WRF computes atmospheric flow by solving equations of motion for compressible and non-hydrostatic flow with the initial and boundary conditions taken from re-analysis data. We have used NCEP FNL Global Analysis data with  $1.0^\circ \times 1.0^\circ$  resolution provided every six hours as the input wind data for WRF, and NCEP Real-Time Global SST analysis data (RTG-SST) with  $\frac{1}{12}^\circ \times \frac{1}{12}^\circ$  resolution provided every 12 hours to update the sea surface temperature. Two-domain nesting computation was performed with the domains shown in Table 2 which are slightly larger than the domains 2–3 of the wave computation. The following options were chosen as the physical parametrisation schemes: Single-moment six-class scheme for the microphysics (Hong and Lim, 2006); rapid radiative transfer model for long

wave radiation (Mlawer et al., 1997); Goddard’s scheme for short wave radiation (Chou and Suarez, 1994); Mesoscale Model (MM5) similarity theory for the surface layer (Zhang and Anthes, 1982); NOAH land surface model (Chen and Dudhia, 2001); Yonsei University scheme for planetary boundary layer (Hong et al., 2006); and Kain-Fritsch scheme for cumulus parametrisation (Kain, 2004). These settings were determined based on the comparison of the computational results with observed data.

## 2.3. Tidal Current Model

Although a large number of global tidal models have been proposed (e.g. FES2004 (Lyard et al., 2006), TPXO7.2 (Egbert and Erofeeva, 2002)) which are able to predict tidal conditions in deep water at high accuracy, the prediction by these models in coastal regions with complex shorelines is known to be less accurate. In the present work, both the tidal current velocity and the tidal sea surface elevation were computed using MOHID Water Modelling System (Martins et al., 2001) developed at the Technical University of Lisbon to provide input into the present wave model. MOHID solves the continuity and momentum equations with Boussinesq

Table 2: Computational conditions for WRF computation.

Domain	Computational area	Grid number	Grid spacing (lon×lat)	$\Delta t$
1	W16.20°–E5.70°, N55.80°–N63.70°	221×81×27	0°6′ × 0°6′	30sec
2	W6.04°–W1.76°, N57.96°–N60.04°	216×106×27	0°1.2′ × 0°1.2′	6sec

approximations in hydrostatic equilibrium. The computational domain used for the tidal model is identical with domain 4 of the wave computation (see Table 1), having a  $360 \times 240$  cell grid with a uniform interval of  $15' \times 15'$  and a time step of 30 seconds. Boundary conditions of the tidal velocity and surface elevation were applied based on the FES2004 global tidal solution with 15 tidal constituents at  $\frac{1}{8}^\circ \times \frac{1}{8}^\circ$  grid resolution, which was obtained from a hydrodynamic computation and data assimilations. While the Coriolis force was included in the computation, no wave or wind effects on the tidal current were considered.

### 3. Validation

For each of the models described above, a validation exercise was conducted by comparing simulated time series with observed data from met-stations and oceanographic instrument deployments. Figure 1 shows the locations used for validation: Wind measurements were taken from met-stations at Stornaway, Kirkwall, Lerwick, Fair Isle and Wick; tidal velocity measurements were used from instruments (T1 and T2) located in the Pentland Firth; wave data came from a waverider buoy (W1) located near the European Marine Energy Centre (EMEC) wave test site.

Figure 2 compares the  $U_{10}$  measured and simulated wind velocity time series at the five met-stations.  $U_{10}$  is defined as the wind velocity at 10 m above the local ground (or sea level).  $U_{10}$  is commonly reported by met-stations and weather satellites and is used as the input wind velocity in the SWAN model. In figure 2 a solid line is used to represent the simulated time series at each met-station, while dots are used for the observers data. In general, there is a good agreement between the overall trend and peak wind velocities at all of the locations, with the correlation coefficients varying between 0.63 and 0.85. For days 5 to 10 the wind speed at Kirkwall is under predicted by the model, whilst the model over predicts the wind speed at Lerwick and Fair Isle over the same period. Because the prevailing wind direction

is from the southwest the influence of this difference on the wave field is small.

Comparisons of the tidal current between the present computational results and observation data at T1 and T2 (see Fig.1) are presented in Fig.3. The correlation coefficients of the time series of the current velocity are 0.79 and 0.71 at T1 and T2, respectively. The average difference between the measured and predicted current velocity is  $0.24\text{ms}^{-1}$  at both locations. Although the differences in the velocity are not insignificant, the overall features of the velocity field, especially local variation depending on bathymetry are thought to be reasonably reproduced.

Figure 4 shows the comparison of significant wave height,  $H_s$ , peak,  $T_p$ , and mean,  $T_m$ , periods and wave direction,  $\theta_w$ , between observation data and the computational results in the simulation with tidal current (case 2). Two days of “spin up” are required from the beginning of the simulation before the errors from the initial conditions have washed out of the simulation and the wave field is fully developed. Once the initial transients have left the domain, the coefficient of correlation is 0.93 and 0.75 between the computed and observed significant wave heights and mean periods, respectively, indicating that an accurate hindcast has been made.

During days 10 to 19 and 21 to 27 days there is much less agreement between the observed data and the simulation, resulting in low correlation coefficients of 0.55 and 0.42 for significant wave height and wave period respectively. During these periods, low significant wave height leads to an unsteady wave spectrum, with fluctuating wave periods and direction. The sea state is undeveloped and as a consequence, is not reproduced accurately in the simulation. Discarding periods when the significant wave height is less than 1.5m leads to correlation coefficients of at least 0.70 in all cases.

### 4. Results

Figure 5 shows the areas leased by the Crown Estate in the UK to developers wishing to exploit the wave and

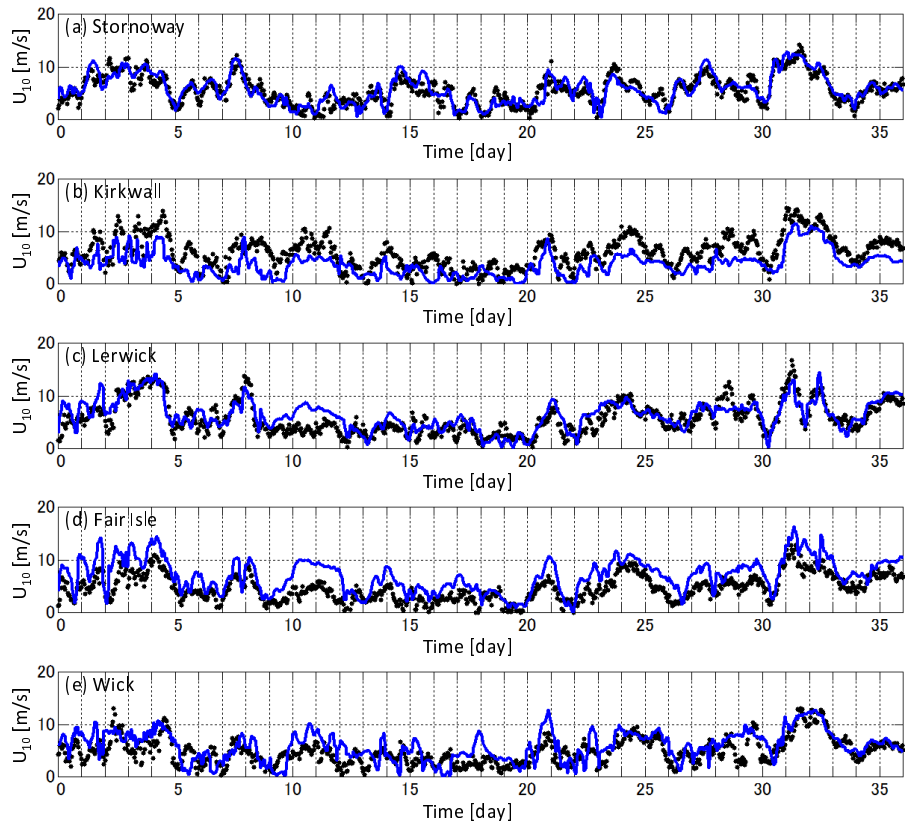


Figure 2: Comparison of 10-m wind velocity  $U_{10}$  between computational results (line) and observed data (dots). Horizontal axes are the time from 2006 July 9, 00:00. Coefficients of correlation were (a) 0.853 (b) 0.739 (c) 0.801 (d) 0.834 (e) 0.625, respectively.

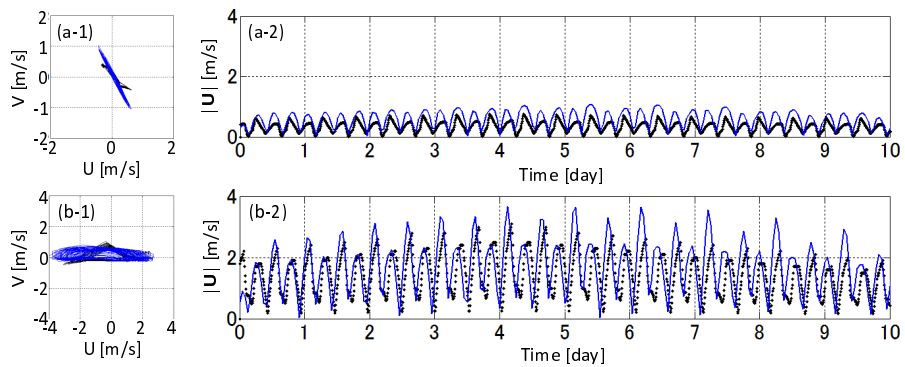


Figure 3: Comparisons between observation data (black) and the present computational results (blue) for tidal ellipses (left) and evolution of absolute tidal current velocity (right) at (a) T1 and (b) T2.

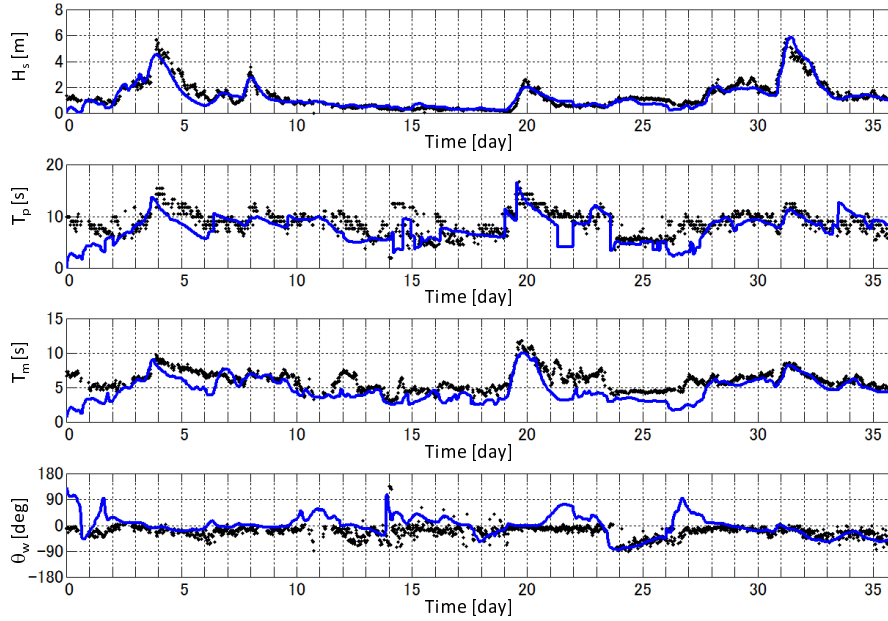


Figure 4: Comparison of significant wave height  $H_s$ , peak period  $T_p$ , mean period  $T_m$  and mean wave direction  $\theta_w$  between computational results (line) and observed data (dots) at the point W1. Horizontal axes are the time from 2006 July 9, 00:00. Buoy data is reproduced with permission of the European Marine Energy Centre Ltd.

tidal resources in the Pentland Firth and Orkney Waters in 2010. These sites represent an ambition by power utilities, project developers and device developers to install 1.6GW of generation capacity before 2025. Two of the leased tidal sites (Westray South and Cantick Head) and one of the wave sites (West Orkney South) are of particular interest in the present work. At three points (Fig. 6) near to these potential deployments the wave-current interactions have been examined in detail. *P1* is located close to the EMEC wave test site at the western entrance to Scapa Flow; *P2* on the northern side of the western end of the Pentland Firth just south of the Island of Hoy; and *P3* at the northwestern end of Westray Sound. These locations are in positions where the maximum current velocity exceeds  $2\text{ms}^{-1}$  while still being subjected to the full force of the Atlantic waves. The selection of these points is motivated both by an analysis of the characteristics of the wave and tidal fields throughout the simulation and the locations of the Crown Estate leases.

Figure 6 shows the mean wave height (averaged over the last 34 days of the simulation) and maximum tidal current velocity over the same period from the combined wave and current simulation (case 2). Eastward of the Orkney islands the wave climate is dominated by the large, long period, Atlantic swell waves which make

the areas so suited to wave energy projects. The sea to the east of the islands is sheltered from the Atlantic swell, but can be subjected to local wind driven seas and lower amplitude swell from the North Sea. As the tide flows between the Atlantic and the North Sea, the narrow channels concentrate and accelerate the flow leading to very high tidal current velocities. To the south, the Pentland Firth between the Scottish mainland and the Orkneys (Figure 6 Region A) experiences the highest velocities. At the western entrance to the Firth the flow is concentrated between the Island of Hoy and the mainland, while at the eastern end the flow is constricted between Brough Ness (on the mainland) and the island of South Ronaldsay. On the southern side of the firth the Island of Stroma divides the flow between the main channel and the Inner Sound. To the north, Westray Sound forms a second channel which concentrates the flow. At the entrance to the Sound (Figure 6 Region B) flow is funnelled between the islands of Westray and Rousay and accelerated. At its southern end the island of Eday deflects the flow accelerating it further. The EMEC tidal test site is located to the south of Eday at the entrance to the Stronsay Firth (southeast of Region B). The third channel considered in the present work is Hoy Sound, which is located between the islands of Hoy and Mainland (the main Orkney Island). Hoy sound

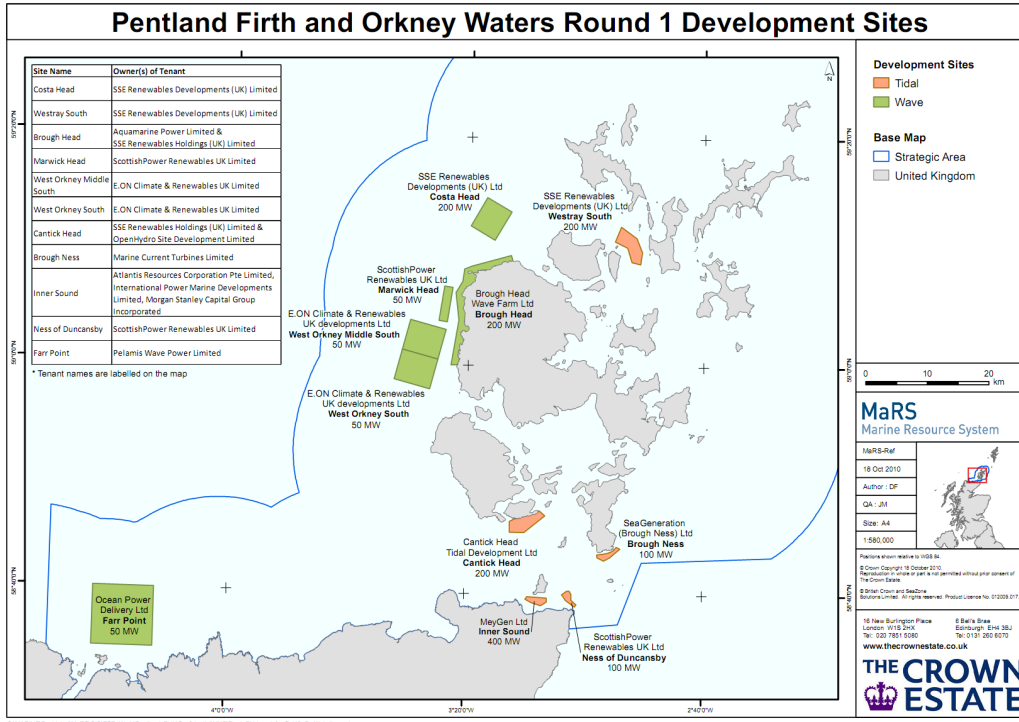


Figure 5: Sites leased for the development of wave and tidal energy projects by the UK Crown Estate in the Pentland Firth and Orkney Waters. Reproduced with permission from The Crown Estate

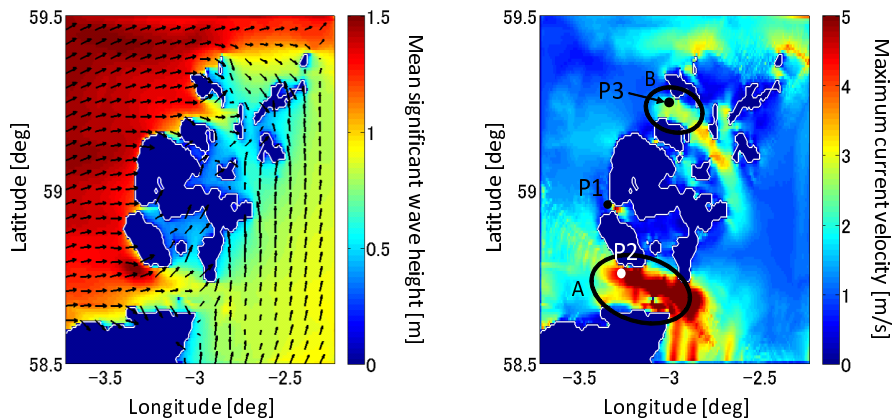


Figure 6: Distributions of (left) mean significant wave height with wave direction and (right) maximum tidal current velocity throughout the computational period. Areas A, B and points P1–P3 are explained in the main text.

forms the western entrance to the large natural harbour of Scapa Flow, whose southern entrance leads into the main channel of the Pentland Firth. Figure 6 also shows the acceleration of the tidal flow around the northern islands of the archipelago, and in several other smaller inter-island channels.

Figure 7 shows the evolution of peak wave period, significant wave height and current velocity during a 9 hour period from 01:00 to 10:00 on day 5 of the simulation (13<sup>th</sup> of July 2006). The four phases illustrated represent the peak westward flow of tidal current (phase 1), slack water at high tide (phase 2), the peak eastward flow of the tide (phase 3), and slack water period at low tide (phase 4). As the westerly tide flows into the Firth (phase 1), the flow is concentrated between the Scottish mainland and the island of Hoy; a similar concentration takes place in the Hoy and Westray Sounds and around the northern islands. During the easterly flood tide (phase 3) the Pentland Skerries and the islands of Muckle Skerry, Swona and Stroma obstruct the flow, concentrating the current in the north of the channel. The westward current in the Firth is consequently faster than the eastward current, as shown in Fig. 3 (b-1). During both of the “slack water” periods there are isolated regions of high current flow; in particular, the current in Hoy Sound persists as water continues to enter and leave Scapa Flow.

Through the simulated period the wave height from the Atlantic swell declines from about 7m to circa 4m. During phase 1, the waves are subjected to a strong current in the same direction as the direction of wave propagation. This lowers the wave amplitude and increases the wave length. Increasing the wave length increases the depth to which the wave motions penetrate the water column - consequently increasing the wave loading on submerged tidal turbines. During the ebb tide (phase 3) the adverse current increases the wave height and shortens the wave length. These effects are particularly pronounced in areas A (Western Pentland Firth) and B (Northern Westray Sound). Because there are still significant currents persisting at high and low water (3 hours after the maximum flood/ebb tide) the influence of the current on the waves is still visible during phases 2 and 4. This is particularly clear during the ebb tide to the south of the island of Hoy.

To further explore the influence of tidal current on the wave field, two separate simulations have been performed. In case 1 the wave field has been computed without the influence of tidal current and in case 2 the tidal current has been included in the simulation. The differences between these simulations (at the points  $P1$ ,  $P2$  and  $P3$ ) on the wave field is shown in Fig. 8 as

scatterplots of  $T_p$  vs.  $H_s$  at each point from the two cases. The scatter plots for case 2 show enhancement of wave height across a range of periods. These differences are particularly marked at  $P2$  (Hoy) and  $P3$  (Westray Sound). The root mean square differences in  $H_s$  and  $T_p$  caused by tidal effects are 0.11m and 0.80s at  $P1$ , 0.82m and 1.66s at  $P2$ , and 0.39m and 1.16s at  $P3$ .

#### 4.1. Characteristics of the Wave Power Field

The wave power (or wave energy flux per metre crest length) (IEC, 2011),  $P$ , may be calculated by the following equation (assuming deep water),

$$P = \frac{\rho g^2}{64\pi} T H_s^2, \quad (4)$$

where  $g$  is the acceleration due to gravity,  $T_e$  is wave energy period and  $H_s$  is significant wave height. The wave power per metre can be computed directly from the SWAN simulations and is shown in figure 9. This figure compares the wave power per metre distributions from the two cases at the same times as phases 1–4 from Fig. 7. Because the wave power per metre varies with the square of the wave height, but only linearly with period, the wave power distribution almost corresponds directly to that of the wave height distributions from figure 9. During the flood tide the wave power is reduced at the entrance to the Pentland Firth and Hoy and Westray Sounds by the tidal current. At high tide the wave power to the south of the Firth is higher than in the wave only case. During the ebb tide wave power is significantly increased in the channels where the current is flowing. This difference persists towards low water, when a localised increase in wave power can be observed to the south of the island of Hoy at the western entrance to the Pentland Firth. A difference in wave power of more than  $100\text{kWm}^{-1}$  is observed due to the interaction of currents and waves.

Figure 10 represents the mean wave power per metre (averaged over the last 34 days of the simulation) computed in the two cases, together with the difference between them. On average the presence of currents increases the mean wave power per metre to the south of Hoy by a maximum of  $7.9\text{kWm}^{-1}$ , with a reduction in  $5.5\text{kWm}^{-1}$  in the main channel of the Firth. The asymmetry in the differences in the mean wave power through the channel is caused by the presence of the islands at the eastern end of the Firth which deflect the ebb current northward. These differences correspond to an increase of 57% and a decrease in 61% of the wave power per metre respectively.

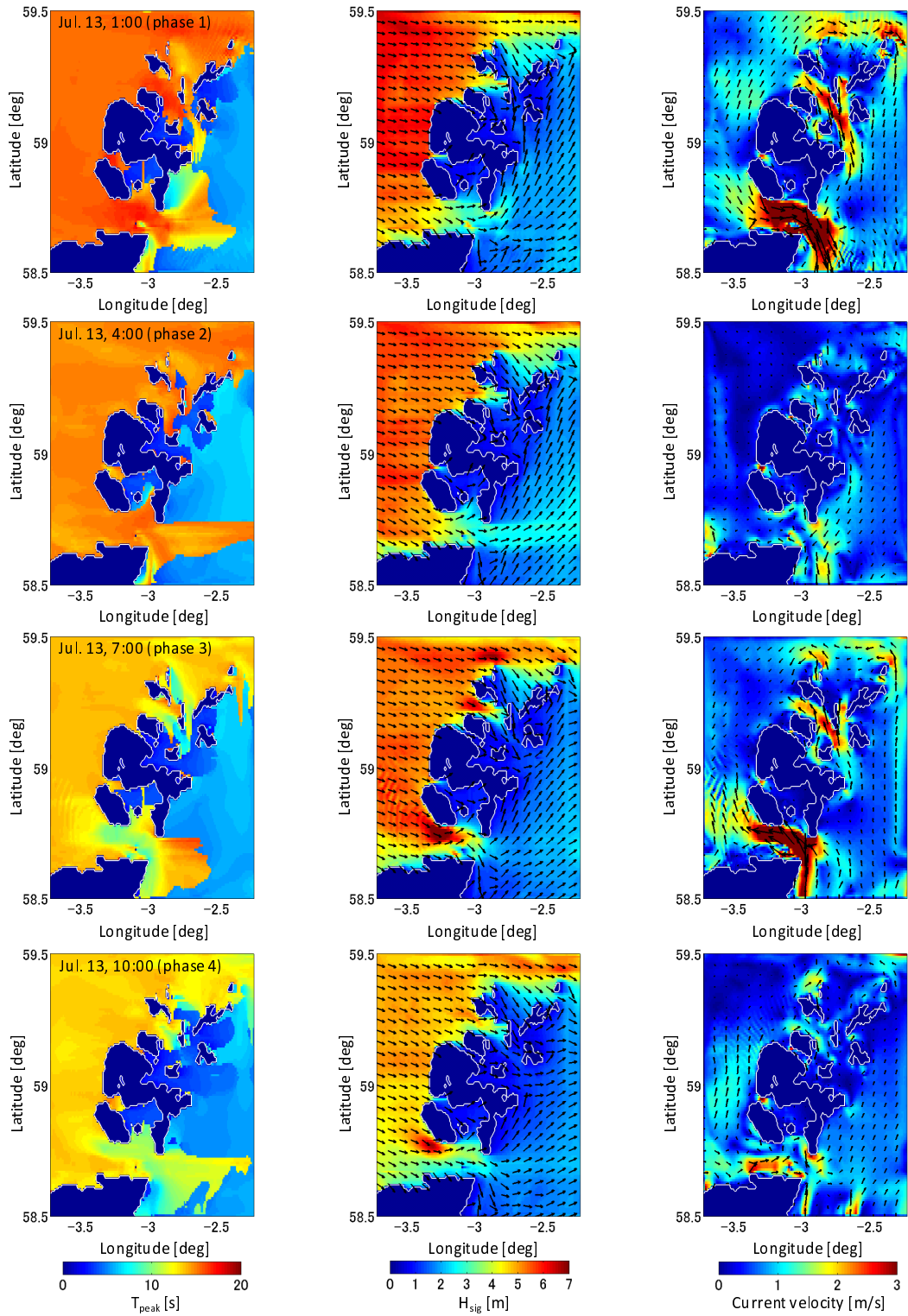


Figure 7: Distributions of (left) peak period, (middle) significant wave height and wave direction, (right) tidal current velocity and its direction from the simulation including tidal current (case 2)

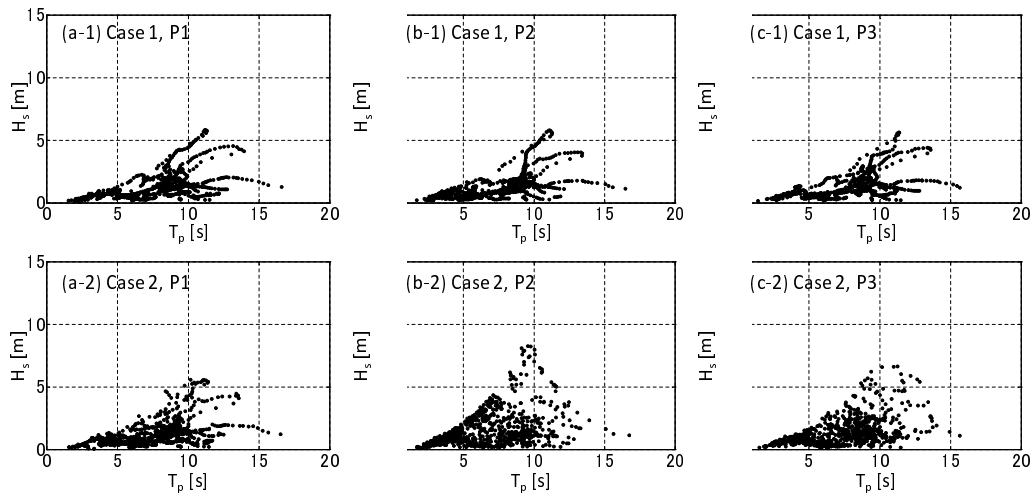


Figure 8: Scatter plots of peak wave period and significant wave height for the wave only simulation (top) and the combined wave and current simulation (bottom) at points P1 to P3.

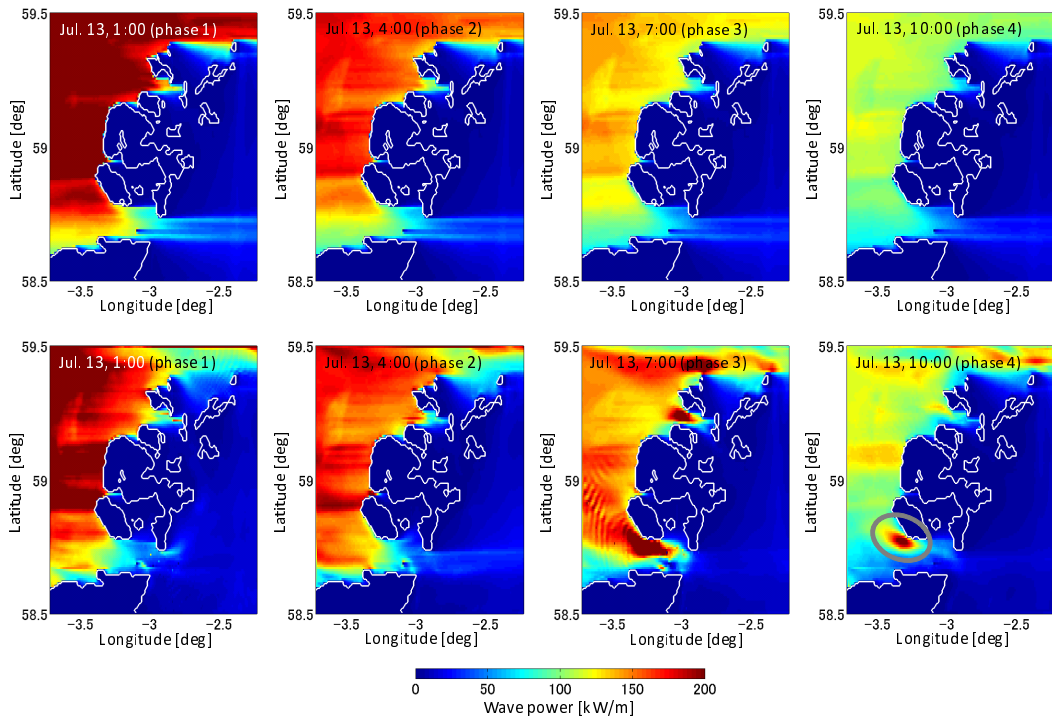


Figure 9: Wave power per metre crest during the maximum flood tide (phase 1), high water (phase 2), maximum ebb tide (phase 3) and low water (phase 4) for the simulation excluding tidal current effects (top) and including tidal current effects (bottom).

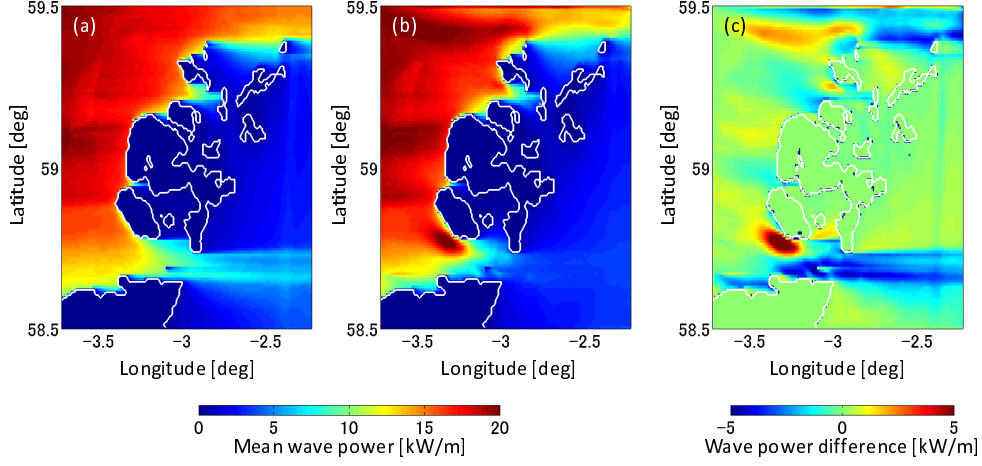


Figure 10: Mean wave power per metre for the simulations without current (left) and with current (middle), together with the difference in the mean wave power between the two cases (right).

## 5. Wave Amplification Diagram

We define the wave amplification factor as

$$\alpha = \frac{H_{m0} |_{tide}}{H_{m0} |_{wave}}, \quad (5)$$

where  $H_{m0} |_{tide}$  is the spectral estimate of the significant wave height in the presence of the tidal current and  $H_{m0} |_{wave}$  is the estimate in the absence of tidal effects. For deep water waves, with a Rayleigh height distribution, this estimate is given by

$$H_{m0} = 4.004 \sqrt{m_0}, \quad (6)$$

where  $m_0$  is the zeroth moment of the wave energy spectrum (Goda, 1985).

$\alpha$  can be computed for a deep water wave travelling into shallower water with a uniform current (Appendix A). Figure 11 shows comparison of wave amplification factor computed using the SWAN simulations at points  $P1$  to  $P3$  with that obtained using this theory. The Figure shows that the theoretical value tends to over-estimate wave amplification under conditions where the small amplitude assumptions break down, due to either a very strong current velocity or a large wave height.

To represent the interaction of waves and currents at a specific location in a format which is helpful for both technology developers and project developers planning deployments, the use of a Wave Amplification Diagram is proposed. In such diagrams (Figure 12) the amplification factor,  $\alpha$ , is plotted as a function of the angle between the incident current direction and the mean wave direction,  $\phi$ .

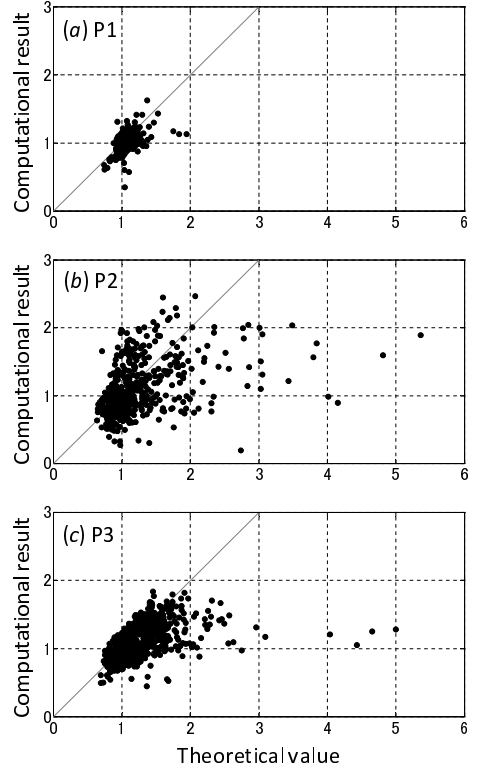


Figure 11: Comparison of wave amplification factor computed in this study with that obtained by small amplification theory.

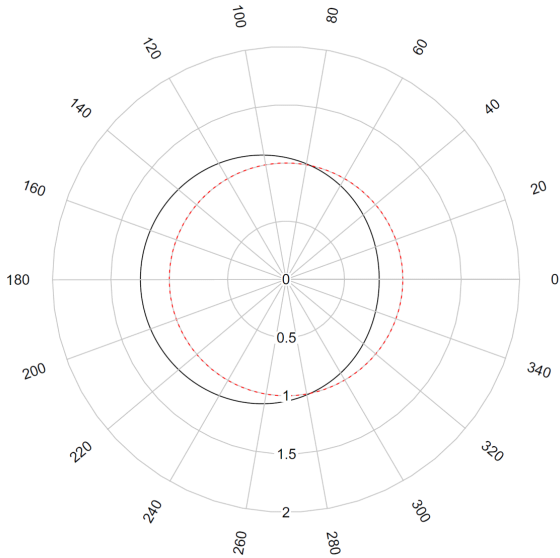


Figure 12: Wave amplification diagram: The ratio of the wave height with and without current are plotted against the relative angle between the mean wave direction and the current (solid line) together with a unit circle (dotted line).

When waves are in crossflow, with the current coming from  $\pm 90^\circ$ , no amplification is expected and the ratio should be approximately 1. When the directions of the current and wave propagation are the same ( $0^\circ$ ) the wave length should increase and the wave height decrease (Peregrine, 1976) leading to  $\alpha < 1$ . When the current and waves are in opposition ( $180^\circ$ ) the wave height increases and the wave length shortens, so  $\alpha > 1$ . For sites where there is limited wave-current interaction the analysis should show that

$$\alpha(\phi) \approx 1 \quad \forall \phi \in [0, 2\pi].$$

Figure 12 shows the amplification factor, computed using small amplitude wave theory (Appendix A), for a 10s period wave propagating into a uniform  $8\text{ms}^{-1}$  current in a depth of 50m. It is worth noting that the combined effects of bathymetry, wave reflection from coastlines, and concentration of tidal current by headlands and narrow channels are likely to result in wave amplification diagrams which do not have symmetry, and where there is less than  $180^\circ$  between the amplified and reduced regions.

For each of the points  $P1$  to  $P3$  the wave amplification factors have been computed using the ratio of the significant wave heights using (5) from the SWAN simulations. These datasets can then be investigated using circular statistical techniques (Fisher, 1993). The

Table 3: Circular mean direction,  $\bar{\theta}$ , circular standard deviation,  $\nu$ , and circular resultant magnitude,  $\bar{R}$ , for the relative wave-current directions for the three locations  $P1$ ,  $P2$  and  $P3$  from the SWAN simulation.

point	$N$	$\bar{\theta}$	$\bar{R}$	$\nu$
P1	818	$313^\circ$	0.131	$115^\circ$
P2	818	$209^\circ$	0.341	$85^\circ$
P3	818	$216^\circ$	0.260	$94^\circ$

analysis presented has been performed using the *circular* statistics tool pack (Agostinelli and Lund, 2011) for the R statistical package (R Development Core Team, 2008). For each of the observations the relative angle between the waves and the current,  $\theta_i$ , is treated as a complex unit vector,  $z = \cos \theta + i \sin \theta$ , and the resultant found,

$$\bar{\rho} = \frac{1}{N} \sum_{i=1}^N z_i. \quad (7)$$

The mean direction (in Radians) is given by,  $\bar{\theta} = \arg \bar{\rho}$ , the mean resultant length,  $\bar{R}$ , associated with the mean direction is defined as  $\bar{R} = |\bar{\rho}|$ , and the sample circular standard deviation (also in Radians) is  $\nu = \sqrt{-2 \ln \bar{R}}$ . These descriptive statistics (with the angles in degrees) are given in Table 3.

Because the mean direction and sample standard deviation are primarily only of use for observations drawn from a single distribution it is important to check if the data is multi-modal. Figure 13 shows circular dot-plots for the three data points with the kernel density estimate (Bai et al., 1988) shown on the same diagram. In the dot-plots the observations are discretised into 120 bins, and for each bin a single dot is plotted for each observation, with subsequent dots in the same bin stacked. In the same way that we expect continuous uni-modal random data to be drawn from the Gaussian distribution, uni-modal circular data is normally modelled by the circular von Mises distribution (Fisher, 1993). In all three cases the plots show the data is multi-modal with one mode located near  $320^\circ$ ; for P1 the second mode is located near  $140^\circ$  while for P2 and P3 the second mode is located near  $180^\circ$ . In no cases is the data unimodal and the Rayleigh test for goodness of fit shows that all three data sets are significantly different from the von Mises distribution at the 5% level. Under these circumstances the circular mean and circular sample standard deviation will not provide good estimates of the centre and spread of the data.

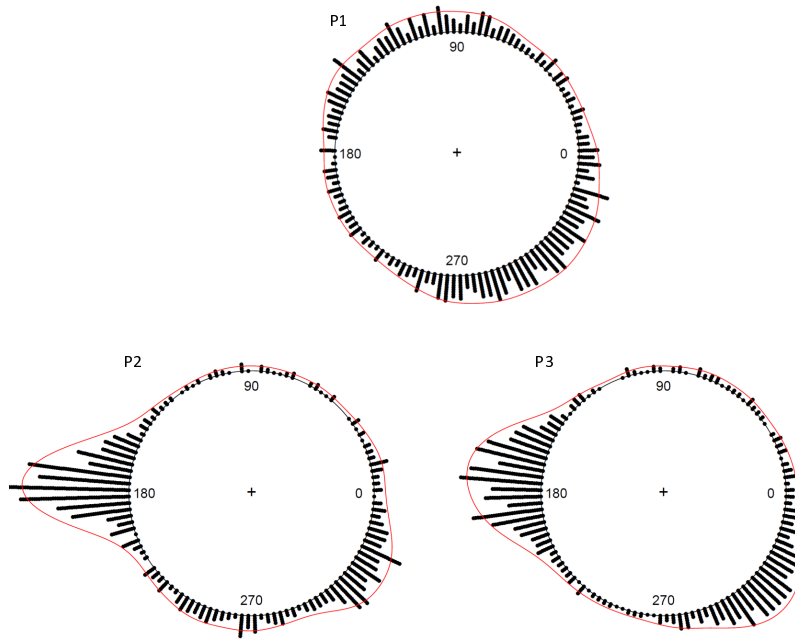


Figure 13: Circular dot-plots of the relative wave-current direction (bar) with the kernel density estimate (line) for P1, P2 and P3.

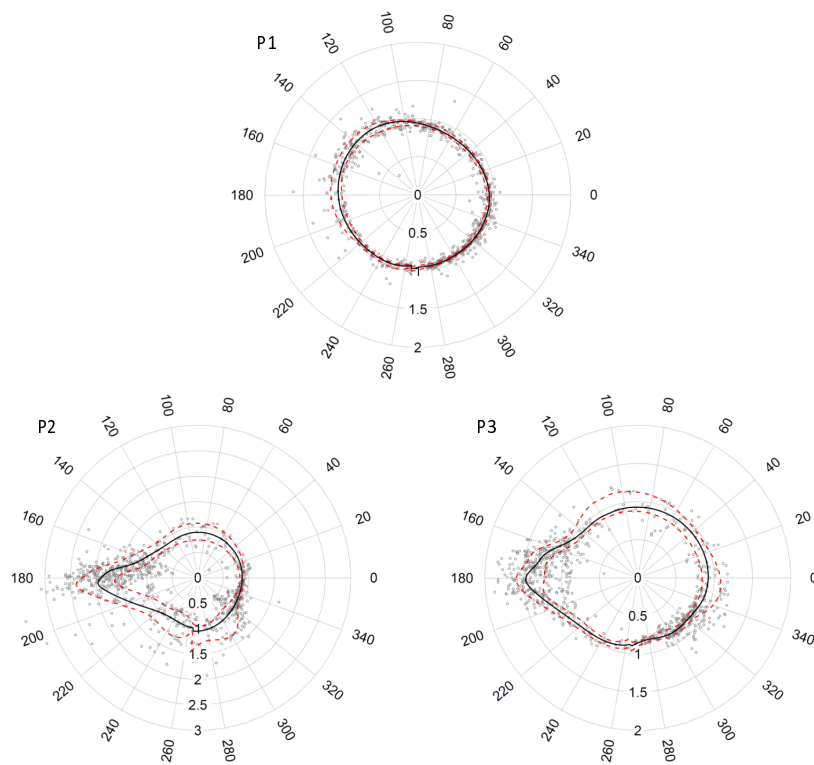


Figure 14: Wave amplification diagrams for P1, P2 and P3. Gray symbols show the individual wave amplification factors, the solid line is the median, and the dashed lines indicate the upper and lower quartiles.

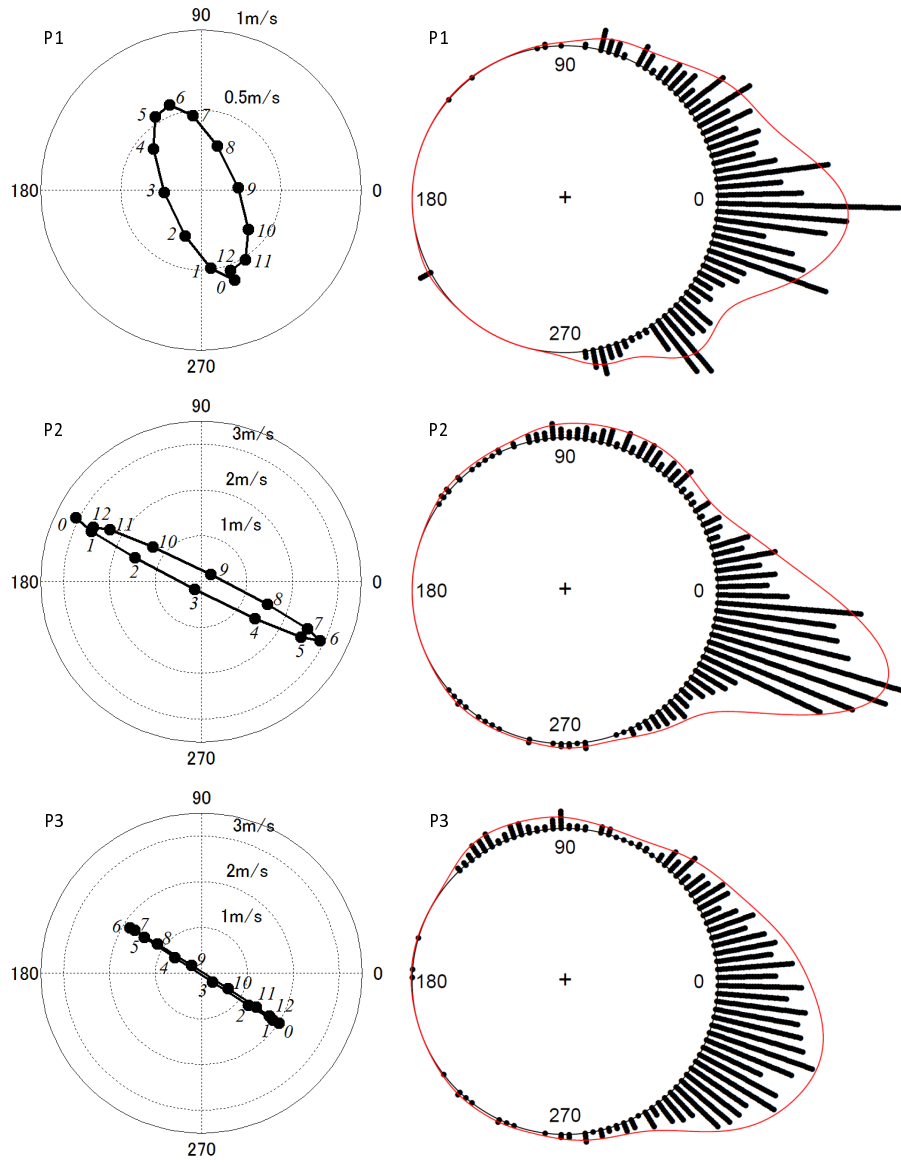


Figure 15: tidal ellipses of M2, S2, K1 and O1 constituents at the spring tide plotted every one hour (left) and circular dot-plots with kernel density estimates of the wave direction (right) at P1, P2 and P3. The angles represent the directions of waves and currents measured counterclockwise from east.

To construct the Wave Amplification Diagrams for the three locations, quantile regression (Koenker and Hallock, 2001) has been used. Quantile regression has a number of advantages over the standard method of least squares in that as well as providing a more robust method in the presence of outliers, it enables fits to be made to specific quantiles of the data. In the present case curves are fitted to the 75<sup>th</sup>, 50<sup>th</sup> and 25<sup>th</sup> quantiles – these are the upper-quartile, median, and lower-quartile of the data sets respectively. Linear quantile regression is based on minimising

$$\sum_{i=1}^n f(y_i - (\alpha_0 + \alpha_1 x_i))$$

where

$$f(y - q) = \begin{cases} \beta(y - q) & y \geq q \\ (1 - \beta)(q - y) & y < q \end{cases}$$

to obtain the  $\beta^{\text{th}}$  quantile. Cubic B-splines (with 15 degree of freedom smoothing) have been fitted using the *quantreg* tool pack for R (Koenker, 2012). In the analysis of circular data, techniques are available for Linear-Circular, Circular-Linear or Circular-Circular regression (see Fisher, 1993). In the present case, the intention is to predict the response variable as a function of angle – Linear-Circular. This case the simplest, where by unwrapping the circular prediction variable, normal regression methods can be applied. One caveat associated with unwrapping in this way is that the fitted curve may be discontinuous at the angle where the "cut" has been made. In the present analysis this approach has been used as there is not currently a package available for circular quantile regression. The observed data has been unwrapped at 265° and discontinuities can be observed in the median and upper quartile curves at this location.

Figure 14 shows a polar scatter plot of the individual observations at each of the three points with the regressed median line in black and the upper and lower quartiles as red dashed lines. The region between the upper and lower quartile lines represents the middle 50% of the observed data for each angle. Using a non-parametric analysis it can be concluded that where this range does not include the unit circle there is significant evidence to show that the wave amplification factor is different from unity.

At *P1* this analysis shows that there is a small but significant reduction in wave amplitude for wave-current angles between 270° and 90°, and a significant increase in wave height between 140° and 180°. This site (Figure

15) is characterised by low current speeds (with a maximum current speed of just over 0.5ms<sup>-1</sup>) and a unimodal wave direction distribution with a median of 0°. These conditions lead to mild wave-current interactions which are consistent with those predicted by the low amplitude theory.

In contrast, *P2*, (see Figure 15) has a strong tidal current of around 3ms<sup>-1</sup> with the mean wave direction coinciding with the major axis of the tidal ellipse ( $\bar{\theta} = 354^\circ, \nu = 38^\circ$ ). The wave amplification diagram (Figure 14) shows a small but significant reduction in amplitude between 320° and 40° and a very large amplification between 160° and 200°. When the current is in exact opposition to the waves the median amplification factor is almost 2. Site *P2* is thus characterised as a site with very large wave-current interactions.

The mean wave direction at *P3* ( $\bar{\theta} = 353^\circ, \nu = 43^\circ$ ) also coincides with the tidal flow directions, although the maximum tidal velocity of 2ms<sup>-1</sup> is less than that at *P2* (Figure 15). This site shows a significant increase in wave amplitude between 160° and 200°, with maximum median amplification factor of 1.5 (Figure 14). The site shows two regions with a significant reduction in wave amplitude, one between 240° and 330°, and a second between 20° and 40°. The reduction in wave amplitude is not significant between 330° and 20° probably due to both the scatter and paucity of the data in this region. *P3* is characterised as a site where the main region of wave height reduction is offset by about 50° (clockwise) from where we would expect — potentially leading to challenges for a wave- or tidal-energy developer utilising the site.

## 6. Conclusion

The effects of the tidal currents on the wave energy resources due to the wave-current interactions were investigated through the computations of wave field around the Orkney Islands by comparing the computational results with and without considering the tidal currents. In the present simulation, wave energy increased and decreased  $\pm 60\%$  at maximum due to the tidal effects in the Pentland Firth, where a strong tidal current of more than 3 m/s is formed. It should be noted that considerable alteration of wave energy can be caused by wave-current interaction at the locations where strong currents coexist with large waves.

The wave amplification diagram was proposed, and the relationship between the wave amplification factor and relative direction of currents on the waves based on the circular analysis with quantile regression was discussed. The basic feature that the waves are amplified

by the currents with the relative direction of 180 degrees (opposing to the waves) and attenuated by the currents with the relative direction of 0 degrees (following to the waves) is seen in the diagrams although different characteristics appear in each diagram depending on the conditions of the waves, currents and geography at the locations. The wave amplification diagram characterises the effects of the wave-current interaction on the wave fields and can be used for better understanding the characteristics of wave energy sites.

## Acknowledgement

We would like to express our gratitude to Dr. Rebecca Killick from the Department of Mathematics and Statistics at Lancaster University for her help and advice on quantile regression and the analysis of linear-circular data. The authors acknowledge the use of buoy data from the European Marine Energy Centre (EMEC) Ltd and of mapping data from the Crown Estate. Support from the European Commission's FP7 project MARINA PLATFORM (Grant Agreement No. 241402) and the EPSRC's GLOBAL - Edinburgh-Pacific Partnership of Excellence in New Energy Technologies project (EP/K004468/1) are also acknowledged.

## Appendix A. Linear waves in current

The amplification factor,  $\alpha$ , for a deep water wave of period,  $T$ , propagating into water of depth,  $d$ , subjected to a uniform current with velocity,  $U$ , can be calculated as follows (Peregrine, 1976; Peregrine and Thomas, 1979):

$$\alpha = \sqrt{\left(1 + \frac{2k'h'}{\sinh 2k'h'}\right)\left(\frac{1}{k'} - u'\right)} + 2u', \quad (\text{A.1})$$

where

$$u' = \frac{UT}{\lambda}, \quad h' = \frac{d\omega^2}{g}, \quad \text{and} \quad k' = \frac{kg}{\omega^2}. \quad (\text{A.2})$$

The wavelength,  $\lambda$ , angular frequency,  $\omega$ , and wave number,  $k$  are defined using the normal linear wave theory definitions:

$$\lambda = \frac{g}{2\pi} T^2 \tanh\left(\frac{2\pi d}{\lambda}\right), \quad (\text{A.3})$$

$$\omega = \frac{2\pi}{T}, \quad (\text{A.4})$$

and,

$$\omega^2 = gk \tanh dk. \quad (\text{A.5})$$

## References

- Agostinelli, C., Lund, U., 2011. R package `circular`: Circular Statistics (version 0.4-3). CA: Department of Environmental Sciences, Informatics and Statistics, Ca' Foscari University, Venice, Italy. UL: Department of Statistics, California Polytechnic State University, San Luis Obispo, California, USA. URL: <https://r-forge.r-project.org/projects/circular/>.
- Bai, Z.D., Rao, C.R., Zhao, L.C., 1988. Kernel estimators of density function of directional data. *Journal of Multivariate Analysis* 27, 24–39.
- Booij, N., Ris, R., Holthuijsen, L., 1999. A third-generation wave model for coastal regions: 1. Model description and validation. *Journal of Geophysical Research* 104, 7649–66.
- Brière, C., Abadie, A., Bretel, P., Lang, P., 2007. Assessment of TELEMAC system performances, a hydrodynamic case study of Anglet, France. *Coastal Engineering* 54, 345–56.
- Brito-Melo, A., Huckerby, J. (Eds.), 2010. Annual Report 2010: Implementing Agreement on Ocean Energy Systems. OES-IA.
- BVG Associates, 2011. Wave and tidal energy in the Pentland Firth and Orkney waters: How the projects could be built. Tech. Rep. 71431. The Crown Estate; 16 New Burlington Place, London W1S 2HX. United Kingdom.
- Chen, F., Dudhia, J., 2001. Coupling an advanced land-surface/hydrology model with the Penn State/NCAR MM5 modeling system. Part I: Model description and implementation. *Mon. Wea. Rev.* 129, 569–85.
- Chou, M.D., Suarez, M.J., 1994. An efficient thermal infrared radiation parameterization for use in general circulation models. NASA Tech. Memo 104606, 85–.
- Egbert, G.D., Erofeeva, S.Y., 2002. Efficient inverse modeling of barotropic ocean tides. *J. Atmos. Oceanic Technol.* 19, 183–204.
- Fisher, N., 1993. *Statistical Analysis of Circular Data*. Cambridge University Press, Cambridge, UK.
- Goda, Y. (Ed.), 1985. *Random seas and maritime structures*. University of Tokyo Press.
- Hong, S.Y., Lim, J.O.J., 2006. The WRF single-moment 6-class microphysics scheme (WSM6). *J. Korean Meteor. Soc.* 42, 129–51.
- Hong, S.Y., Noh, Y., Dudhia, J., 2006. A new vertical diffusion package with an explicit treatment of entrainment processes. *Mon. Wea. Rev.* 134, 2318–41.
- IEC, 2011. *Marine Energy – Wave, tidal and other water current converters – Part 1: Terminology*. Technical Specification 62600-1. International Electrotechnical Commission. Geneva, Switzerland.
- Ingram, D., Smith, G., Bittencourt Ferreira, C., Smith, H. (Eds.), 2011. *Protocols for the Equitable Assessment of Marine Energy Converters*. The University of Edinburgh, Edinburgh, United Kingdom.
- Kain, J.S., 2004. The Kain-Fritsch convective parameterization: An update. *J. Appl. Meteor.* 43, 170–81.
- Koenker, R., 2012. R package `quantreg`: Quantile Regression (version 4.81). University of Illinois at Urbana-Champaign, Champaign, Illinois, USA. URL: <http://cran.r-project.org/web/packages/quantreg>.
- Koenker, R., Hallock, F., 2001. Quantile regression. *Journal of Economic Perspectives* 15, 143–56.
- Lyard, F., Lefevre, F., Letellier, T., Francis, O., 2006. Modelling the global ocean tides: Modern insights from FES2004. *Ocean Dynamics* 56, 394–415.
- Martins, F., Leitao, P., Silva, A., Neves, R., 2001. 3D modelling in the Sado estuary using a new generic vertical discretization approach. *Oceanologica Acta*, suppl. S 24, S51–62.
- Mlawer, E.J., Taubman, S.J., Brown, P.D., Iacono, M.J., Clough, S.A., 1997. Radiative transfer for inhomogeneous atmosphere: RRTM,

- a validated correlated-k model for the longwave. *J. Geophys. Res.* 102, 16663–82.
- Peregrine, D., 1976. Interaction of water waves and currents. *Advances in Applied Mechanics* 16, 9–117.
- Peregrine, D., Thomas, G., 1979. Finite-amplitude deep-water waves on current. *Philosophical Transactions of the Royal Society of London. Series A, Mathematical and Physical Sciences* 292, 371–90.
- R Development Core Team, 2008. *R: A Language and Environment for Statistical Computing*. R Foundation for Statistical Computing. Vienna, Austria. URL: <http://www.R-project.org>. ISBN 3-900051-07-0.
- Ris, R., Holthuijsen, L., Booij, N., 1999. A third-generation wave model for coastal regions: 2. Verification. *Journal of Geophysical Research* 104, 7667–81.
- Sørensen, O.R., Kofoed-Hansen, H., Rugbjerg, M., Sørensen, L., 2004. A third generation spectral wave model using an unstructured finite volume technique, in: Smith, J.M. (Ed.), *Coastal Engineering 2004: Proceedings of the 29th International Conference*, World Scientific. pp. 894–906.
- van der Westhuysen, A.J., Zijlema, M., Battjes, J.A., 2007. Nonlinear saturation-based whitecapping dissipation in swan for deep and shallow water. *Coastal Engineering* 54, 151–70.
- Zhang, D.L., Anthes, R.A., 1982. A high-resolution model of the planetary boundary layer-sensitivity tests and comparisons with SESAME-79 data. *J. Appl. Meteor.* 21, 1596–609.